Early Results From GLASS-JWST. XII. The Morphology of Galaxies at the Epoch of Reionization

T. Treu[1], A. Calabrò[2], M. Castellano[2], N. Leethochawalit[3,4,5], E. Merlin[2], A. Fontana[2], L. Yang[6], T. Morishita[7], M. Trenti[3,4], A. Dressler[8], C. Mason[9,10], D. Paris[2], L. Pentericci[2], G. Roberts-Borsani[1], B. Vulcani[11], K. Boyett[3,4], M. Bradac[12,13], K. Glazebrook[14], T. Jones[13], D. Marchesini[15], S. Mascia[2], T. Nanayakkara[14], P. Santini[2], V. Strait[9,10], E. Vanzella[16], and X. Wang[7]

[1] Department of Physics and Astronomy, University of California, Los Angeles, 430 Portola Plaza, Los Angeles, CA 90095, USA; tt@astro.ucla.edu
[2] INAF Osservatorio Astronomico di Roma, Via Frascati 33, I-00078 Monteporzio Catone, Rome, Italy
[3] School of Physics, University of Melbourne, Parkville 3010, VIC, Australia
[4] ARC Centre of Excellence for All Sky Astrophysics in 3 Dimensions (ASTRO 3D), Australia
[5] National Astronomical Research Institute of Thailand (NARIT), Mae Rim, Chiang Mai, 50180, Thailand
[6] Kavli Institute for the Physics and Mathematics of the Universe, The University of Tokyo, Kashiwa, 277-8583, Japan
[7] Infrared Processing and Analysis Center, Caltech, 1200 E. California Blvd., Pasadena, CA, 91125, USA
[8] The Observatories, The Carnegie Institution for Science, 813 Santa Barbara St., Pasadena, CA, 91101, USA
[9] Cosmic Dawn Center (DAWN), Denmark
[10] Niels Bohr Institute, University of Copenhagen, Jagtvej 128, DK-2200 Copenhagen N, Denmark
[11] INAF Osservatorio Astronomico di Padova, vicolo dell'Osservatorio 5, I-35122 Padova, Italy
[12] University of Ljubljana, Department of Mathematics and Physics, Jadranska ulica 19, SI-1000 Ljubljana, Slovenia
[13] Department of Physics and Astronomy, University of California Davis, 1 Shields Avenue, Davis, CA, 95616, USA
[14] Centre for Astrophysics and Supercomputing, Swinburne University of Technology, PO Box 218, Hawthorn, VIC 3122, Australia
[15] Department of Physics and Astronomy, Tufts University, 574 Boston Ave., Medford, MA, 02155, USA
[16] INAF—OAS, Osservatorio di Astrofisica e Scienza dello Spazio di Bologna, via Gobetti 93/3, I-40129 Bologna, Italy

Abstract

Star-forming galaxies can exhibit strong morphological differences between the rest-frame far-UV and optical, reflecting inhomogeneities in star formation and dust attenuation. We exploit deep, high-resolution, NIRCAM seven-band observations to take a first look at the morphology of galaxies in the epoch of reionization ($z > 7$), and its variation in the rest-frame wavelength range between Lyα and 6000–4000 Å, at $z = 7$–12. We find no dramatic variations in morphology with wavelength—of the kind that would have overturned anything we have learned from the Hubble Space Telescope. No significant trends between morphology and wavelengths are detected using standard quantitative morphology statistics. We detect signatures of mergers/interactions in 4/19 galaxies. Our results are consistent with a scenario in which Lyman-break galaxies—observed when the universe is only 400–800 Myr old—are growing via a combination of rapid, galaxy-scale star formation supplemented by the accretion of star-forming clumps and interactions.

Unified Astronomy Thesaurus concepts: High-redshift galaxies (734)

1. Introduction

For more than a century it has been known that galaxies in the local universe do not come in every size, shape, and form (e.g., Hubble 1926). Rather, they can be easily classified into a small number of shapes, namely ellipticals, spirals, lenticulars, and irregulars. Galaxy morphology is the result of the underlying astrophysical process governing galaxy formation and evolution. A longstanding goal of extragalactic astronomy has been to explain why galaxies appear the way they do (see Conselice 2014 and references therein).

One of the major results of the Hubble Space Telescope (HST) has been that galaxy morphologies evolve with cosmic time, with classical elliptical and spiral galaxies dominating below $z \sim 1$ and irregular and merging galaxies being more and more common at higher redshifts (e.g., Lee et al. 2013). Structural properties and merger fractions have been investigated in the optical rest frame up to redshift $z \sim 3$ through imaging in the F814W, F105W, F125W, and F160W HST

filters (Bond et al. 2011; Law et al. 2012; Morishita et al. 2014; van der Wel et al. 2014; Huertas-Company et al. 2016; Whitney et al. 2021).

However, at $z > 3$ morphological studies become difficult. The optical rest frame shifts beyond the reach of HST's Wide Field Camera 3 (WFC3), forcing one to rely on rest-frame UV light. Several works indeed extend the analysis of galaxy size and morphology at $z > 3$ in this wavelength regime (e.g., Conselice & Arnold 2009; Shibuya et al. 2015; Ribeiro et al. 2016; Bowler et al. 2017). However, UV light is dominated by young stars and might therefore capture the location of star-forming regions rather than the morphology of the bulk of stellar mass traced by more mature stars (see, e.g., Rawat et al. 2009, for a discussion of this effect). Furthermore, cosmological surface brightness dimming, limited angular resolution, and poor sampling of the WFC3-IR channel degrade significantly even when UV rest-frame information is available. These effects, sometimes referred to as the "morphological" K-correction (Kuchinski et al. 2001; Wuyts et al. 2012), can be substantial in terms of quantitative morphology.

Our morphological ignorance is particularly acute for galaxies at the epoch of reionization ($z \sim 7$ and above). Only the far-UV rest frame is accessible to HST, and their sizes are

so compact that they are typically only marginally resolved by WFC3 (e.g., Oesch et al. 2010; Grazian et al. 2012). Strong lensing magnification helps with the angular resolution (e.g., Yang et al. 2022a), but cannot overcome the limitations in wavelength coverage. At last, with JWST we can overcome these limitations by virtue of its superior angular resolution and longer wavelength coverage with respect to HST.

We use images obtained with NIRCam (Rieke et al. 2005) on board the James Webb Space Telescope as part of the GLASS-JWST ERS program (Treu et al. 2022) to take a first look at the morphology of $z > 7$ galaxies. Our goal is to give a first answer to the questions "What do galaxies at $z > 7$ look like in the optical rest frame?" and "Are the UV and optical rest-frame morphologies of $z > 7$ galaxies similar or vastly different?" by applying well-established quantitative morphological methods to the revolutionary data set. The seven-band imaging data set covers observed wavelengths from 0.8 to 4.8 μm, including the rest-frame range between Lyα and $\sim$4000 Å up to $z \sim 12$ (and up to 6000 Å at $z \sim 7$). The resolution (FWHM 0″04–0″14) and sampling (0″031–0″063) are superior to HST in the overlapping regions and comparable all the way to the reddest band. Given the relatively small number of galaxies at $z > 8.5$ in a single NIRCAM pointing, in this initial study we do not consider evolutionary effects above $z = 7$, leaving the investigation of possible differences as a function of redshift to future work, based on larger samples. Two companion papers in the same focus issue discuss the size–luminosity relation of galaxies at $z > 7$ (Yang et al. 2022b) and the morphology of galaxies after reionization is completed (Jacobs et al. 2022).

This letter is organized as follows. In Section 2 we summarize our sample selection. In Section 3 we summarize our quantitative morphological parameters. In Section 4 we present our results. We discuss them in Section 5. We conclude in Section 6. Magnitudes are given in the AB system and a standard cosmology with $\Omega_{\rm m} = 0.3$, $\Omega_{\Lambda} = 0.7$, and $h = 0.7$ is assumed when necessary.

2. Data and Sample Selection

We use NIRCam data obtained in parallel to NIRISS (Doyon et al. 2012) on 2022 June 28–29. Details of the NIRCAM data quality, reduction, and photometric catalog creation can be found in the paper by Merlin et al. (2022; Paper II). Details of the NIRISS observations and data processing can be found in the paper by Roberts-Borsani et al. (2022; Paper I).

After initial processing, samples of galaxies at $z > 7$ are selected according to the "drop-out" technique, as described by Leethochawalit et al. (2022; Paper X) and Castellano et al. (2022; Paper III), supplemented by photometric redshifts. In total, our sample consists of 13 galaxies selected from Paper X and six galaxies from Paper III. The 19 galaxies in our sample span a redshift range approximately from 7 to 12.

A color image gallery of our sample is presented in Figure 1, where for each galaxy we show one color image based on the short wavelength (SW) camera using the F115W, F150W, and F200W bands, and one based on the three long wavelength (LW) channels, F270W, F356W, and F444W. Image cutouts in each individual band are shown in Figure 2. We do not show the F090W band because galaxies at this redshift are undetected owing to the opacity of the intergalactic medium. We notice that two galaxies of the sample presented by Leethochawalit et al. (2022) are likely interacting, so they are

shown together in Figures 1 and 2, and the morphological parameters are calculated for the pair.

3. Methods

3.1. Definitions

For each band, at its original resolution, we derive five well-established quantitative morphological statistics according to the definitions introduced by previous works. The definitions are given below for convenience of the reader and to set the notation.[17]

First, we define a segmentation map for each object. Segmentation maps have been introduced in this context to reduce the impact of noise in the images and increase the signal from low surface brightness regions. They are also recommended when dealing with the relatively low signal-to-noise ratio (S/N) expected for our galaxies (Pawlik et al. 2016). In practice, we apply a 6×6 uniform filter to the images and then derive a segmentation map with the *photutils* astropy package, requiring for the sources at least five connected pixels with a flux of 2σ above the background. We finally define the binary detection mask of the object ($M_{\rm D}$) as the segmentation region corresponding to our target (i.e., removing neighbors or noninteracting companions). From $M_{\rm D}$ we also derive the galaxy radius $R_{\rm max}$ as the maximum pixel distance from the centroid of the binary detection mask (i.e., the pixel coordinates that minimize the shape asymmetry), which works better than the typical Petrosian radius in case of disturbed morphological shapes and low S/N (Pawlik et al. 2016).

The Gini structural parameter (G) quantifies the degree of inequality of the light distribution in a galaxy (Abraham et al. 2003; Lotz et al. 2004), and is defined as:

$$G = \frac{1}{\bar{X} n (n - 1)} \sum_i^n (2i - n - 1) X_i, \tag{1}$$

where n is the number of pixels assigned to the galaxy by the binary detection mask, X_i are the intensities in each pixel i (sorted in increasing order), and $\bar{X}$ is the mean pixel intensity. Gini ranges between 0 (all the pixels have the same intensity) and 1 (all the flux of the galaxy is concentrated in one pixel).

M_{20} is defined as the normalized second order moment of the brightest 20% pixels of the galaxy (Lotz et al. 2004) :

$$M_{20} = \log_{10}\left(\frac{\sum_i M_i}{M_{\rm tot}}\right), \ \ {\rm with} \sum_i f_i < 0.2 f_{\rm tot},$$

$${\rm with} \ M_{\rm tot} = \sum_i^n M_i = \sum_i^n f_i \left[(x_i - x_c)^2 + (y_i - y_c)^2\right], \tag{2}$$

where x_i and y_i are the pixel coordinates (inside the detection mask), while x_c and y_c correspond to the galaxy center where $M_{\rm tot}$ is minimized. f_i are the pixel intensities, while $f_{\rm tot}$ is the total flux of the galaxy within $R_{\rm max}$. This quantity increases with the number of off-centered bright features—with typical values being in the range from -3 to 0—and is usually anticorrelated with concentration.

---

[17] The codes used for the derivation of morphological parameters are fully accessible on the GitHub repository: https://github.com/Anthony96/JWSTmorph.git.
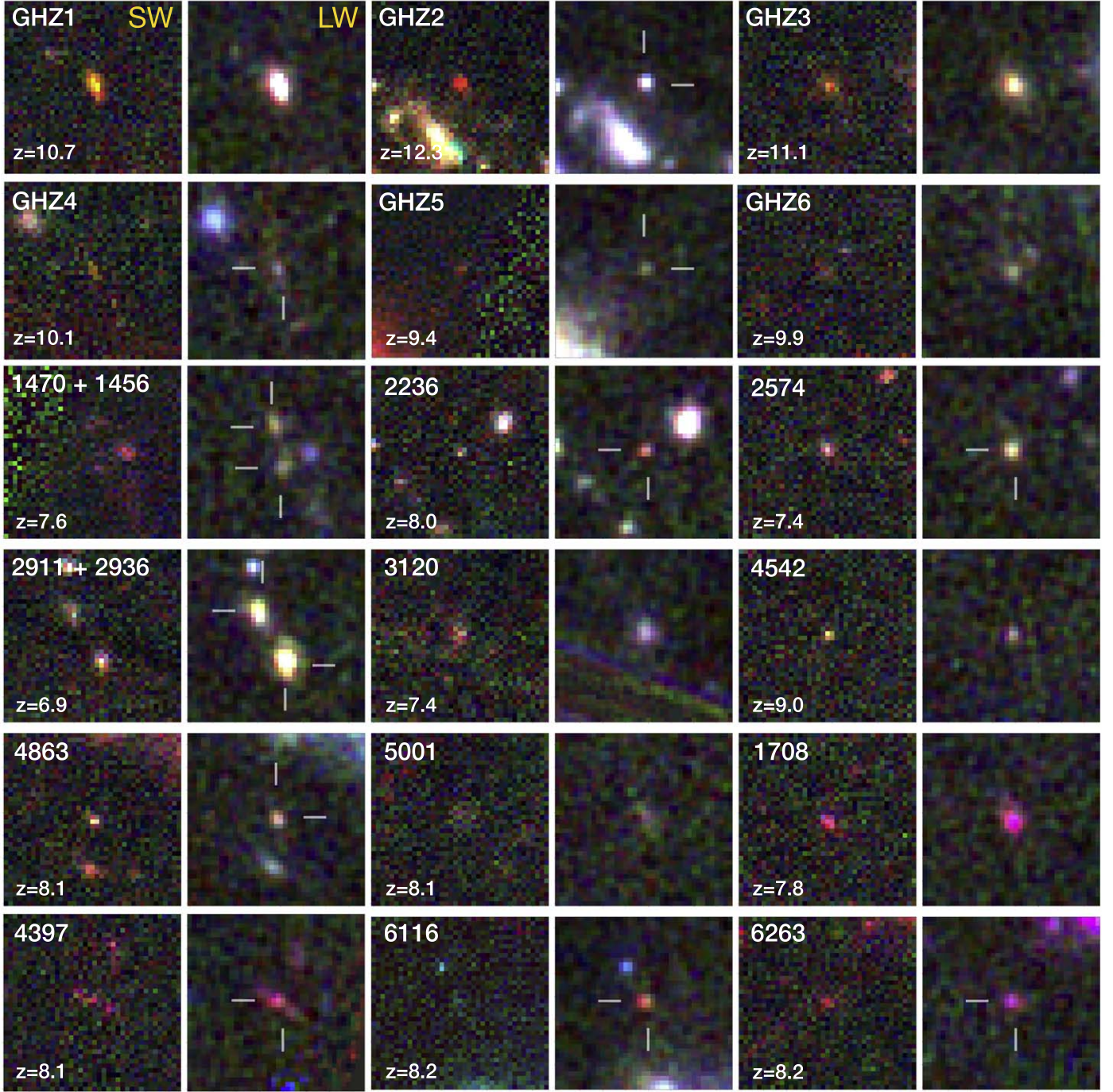
Figure 1. For each galaxy we show a color composite image based on the SW camera ($B = $ F115W, $G = $ F150W, and $R = $ F200W) and one based on the LW camera ($B = $ F277W, $G = $ F356W, and $R = $ F444W). Individual images are degraded to the lower resolution of each camera (i.e., F200W and F444W, respectively). Postage stamps are 2″.4 on a side. Pixels are 31 mas and 63 mas, respectively, for the SW and LW images.

The concentration of light (C) is calculated as in Pawlik et al. (2016):

$$C = 5 \times \log_{10}\left(\frac{R_{80}}{R_{20}}\right), \quad (3)$$

where R_{80} and R_{20} are the radii (from the same center used for R_{max}) enclosing 20% and 80% of the total galaxy flux defined above, respectively.

Shape asymmetry (A_S) is defined by Pawlik et al. (2016) as:

$$A_S = \frac{\Sigma|M_D - M_\pi|}{2 \, \Sigma M_D}, \quad (4)$$

i.e., the difference between the binary detection mask M_D and the same mask rotated by 180° (dubbed M_π), summed over all the cutout pixels, and then divided by the number of pixels of the detection mask multiplied by 2. The center of rotation is taken as the pixel coordinate for which A_S is minimized.
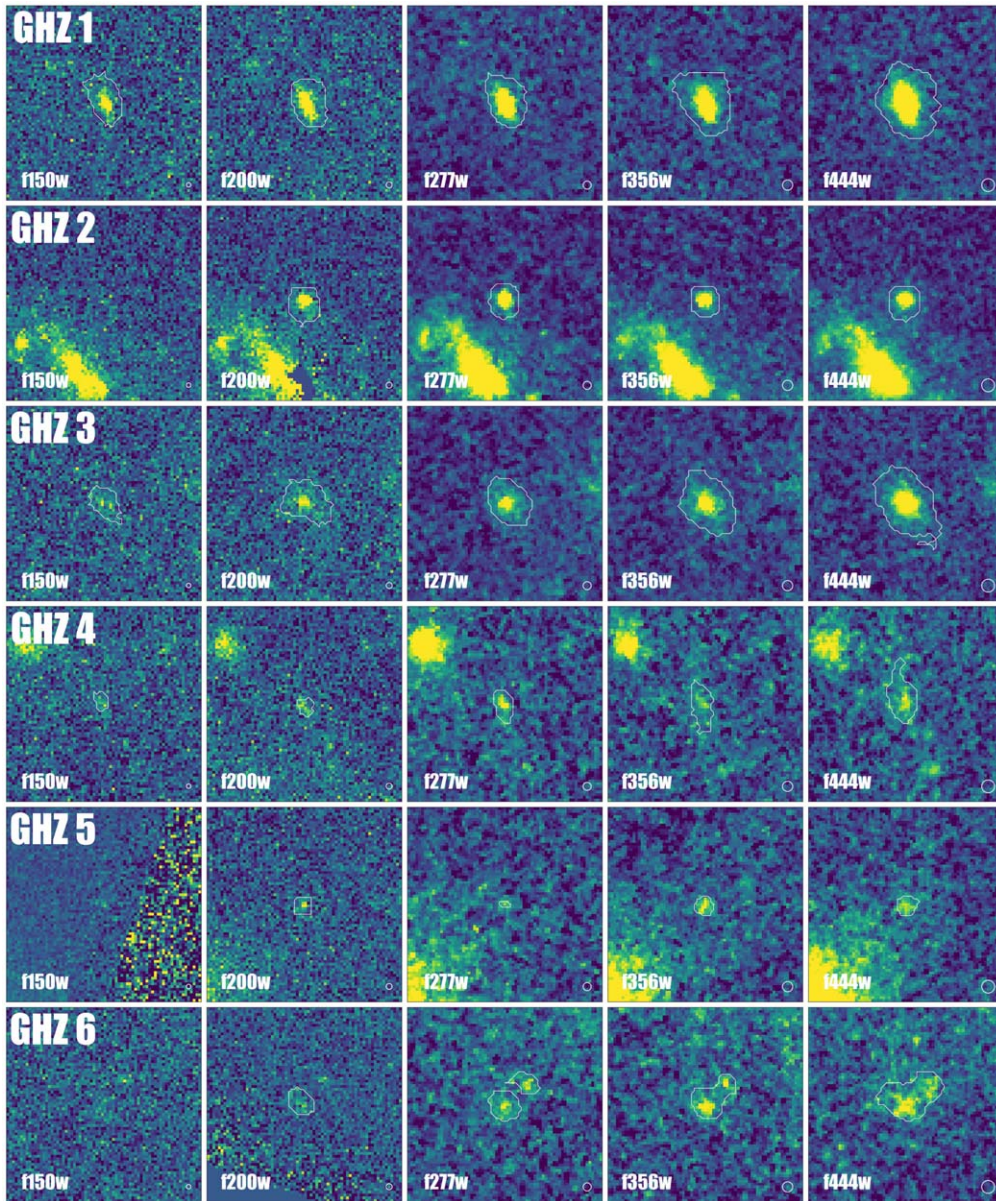
Figure 2. (a) Single-band images of galaxies at $z > 7$ selected by Castellano et al. (2022; Paper III) and Leethochawalit et al. (2022; Paper X), in order of increasing wavelength of observation. The galaxies are identified by the IDs used in Paper III and Paper X. Each postage stamp is $2''.2$ on a side. The images are at their native resolution. Missing stamps are due to artefacts and edge effects. The white continuous lines delimitate the binary detection mask. The circles in the bottom right corner of each band are representative of the PSF FWHM size. In this first part of the figure are shown galaxies at $z \sim 9$–12 from Paper III (Castellano et al. 2022). (b) Galaxies at $z \sim 7$–9 from Paper X (Leethochawalit et al. 2022). Part 1. (c) Galaxies at $z \sim 7$–9 from Paper X (Leethochawalit et al. 2022). Part 2.

Compared to the standard definition of rotational asymmetry (Abraham et al. 1996; Conselice et al. 2003), A_S is purely a measure of morphological asymmetry, regardless of the light distribution inside the galaxy. It is more sensitive to low surface brightness features (Pawlik et al. 2016), and therefore more appropriate for our goal of characterizing the shape of faint galaxies observed at $z \geqslant 7$.

Finally, we also derive the smoothness parameter (S, sometimes called *clumpiness*), which quantifies the contribution of small-scale structures in a galaxy, as defined by Conselice et al. (2003):

$$S = \frac{\Sigma|I_0 - I_\sigma|}{\Sigma|I_0|} - S_{bkg} \qquad (5)$$

where I_0 is the original galaxy image and I_σ is derived by smoothing I_0 with a Gaussian filter, with σ corresponding to a physical size of 1 kpc in the source reference frame. Here, S_{bkg} is the smoothness of the background. A completely smooth light distribution in a galaxy without bright small-scale structures has $S = 0$. Owing to the compact nature of our sources, we do not attempt to identify a central nucleus or to remove the central galaxy regions in the computation of S.

In order to minimize selection and evolutionary effects, we consider differential effects only; i.e., we focus on the variations of each index with wavelength. In practice, for each galaxy and each index, we compute ΔIndex as the difference between the measurement in a given filter and that obtained through F444W.
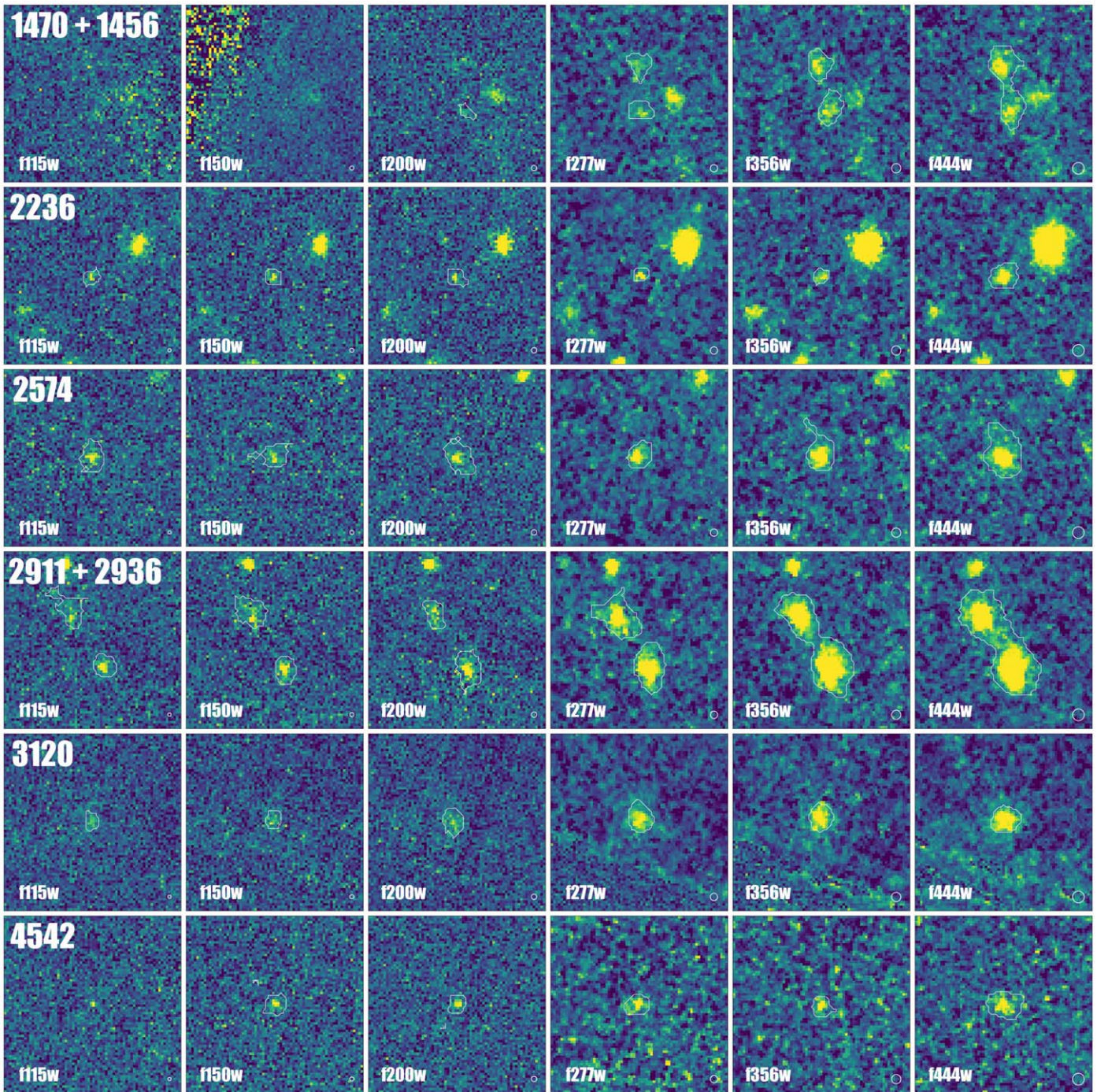
Figure 2. (Continued.)

3.2. Simulations

In order to carry out a meaningful investigation of the variation of these statistics with wavelength, we have to estimate the amplitudes of systematic uncertainties stemming from variations in resolution and pixel size across the NIRCAM bands, and from the effects of correlated noise when matching resolution. We proceed as follows.

First, we simulate images in the F090W, F200W, F277W, and F444W bands, corresponding to the bluer and redder bands of the SW and LW channels, respectively. We note that this is conservative, since in practice we do not use the F090W bands.

Second, we inject Gaussian sources in a set of configurations, aimed at sampling a range of shapes, geometries, sizes, and S/Ns, comparable to those of the expected real sources. In practice, we vary the total number of sources or clumps (from 2 to 4), their size (from 0.5 to 2 kpc at a redshift of 7), their relative position and brightness, the maximum angular extension of the configuration (from $0\rlap{.}{''}2$ to $0\rlap{.}{''}5$), and the total magnitude of the object (26, 27, and 28 AB). In addition, we simulate single sources with a Sérsic profile, varying the Sérsic index from 0.5 to 4, the ellipticity from 0 to 1, and the size and total magnitude as above. In total, we simulate $144 + 120$ different configurations. We also assume for simplicity that the
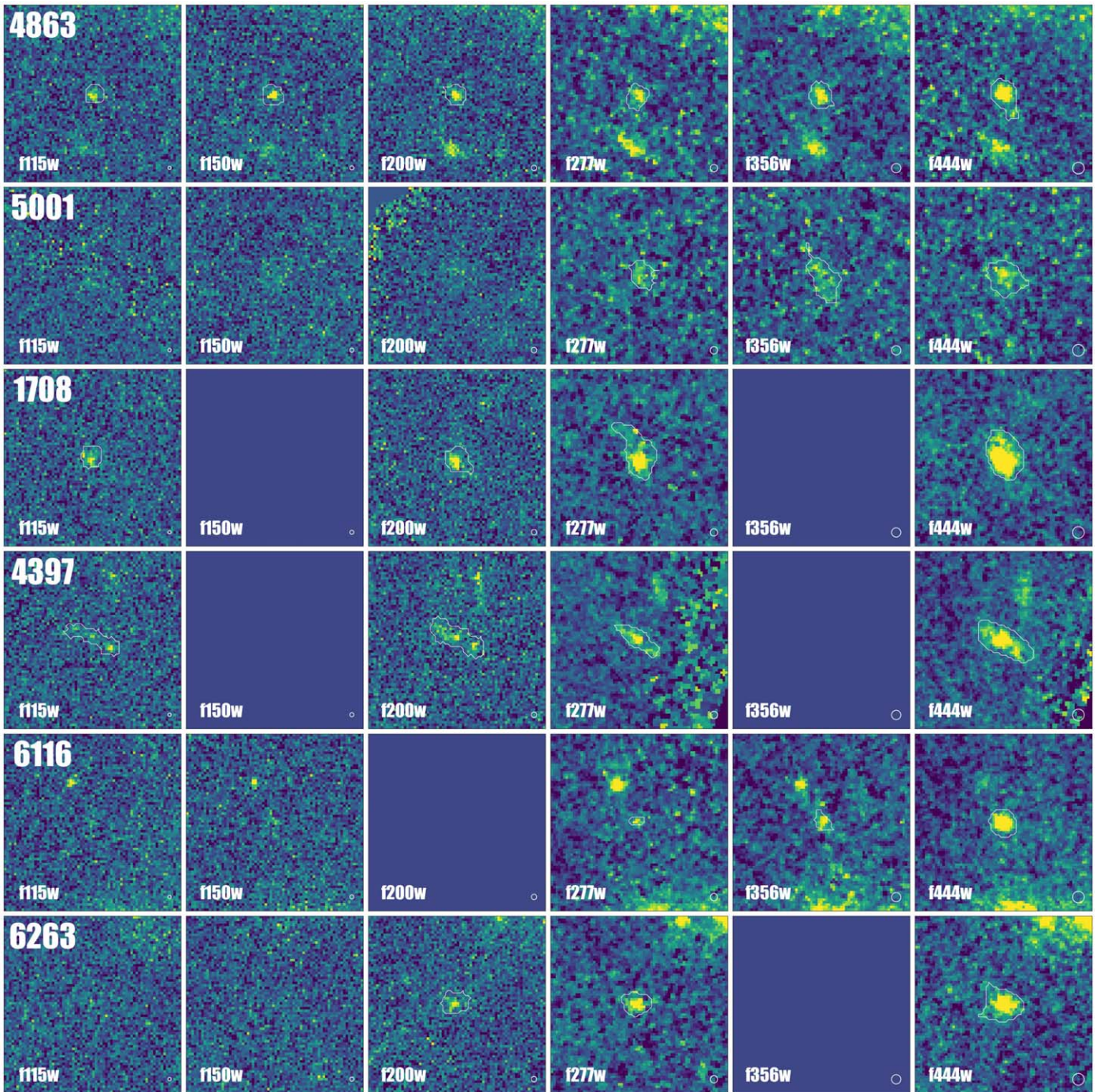
Figure 2. (Continued.)

sources have a flat spectrum in f_ν. For each band and configuration, we create 10 images each with a different realization of the noise. Four of the configurations tested are displayed in each row of Figure 3 as an illustration.

Third, we create mock observations by adding shot noise and background noise, which are estimated in each band from the JWST ETC (v1.7), considering the integration times scheduled for our program (i.e., ∼12,300, ∼5200, ∼5200, and ∼21,000 s from the bluer to the redder bands; Treu et al. 2022). These correspond to the first, third, fourth, and sixth panel of each row in Figure 3. In addition, we downgrade the resolution of our images by convolving them with a Gaussian kernel in order

to match the point-spread function (PSF) size to the redder bands (i.e., from 0″035 to 0″065 for the SW detector, and from 0″09 to 0″14 for the LW detector). This exercise allows us to determine how much the morphological parameters change when introducing correlated noise and lowering the resolution. The convolved images are shown in Figure 3 in the second and fourth panel of each row.

Fourth, we measure the morphological parameters for all the simulated images in each configuration, and compute the differences with respect to the reddest band, as done for the observations. For each parameter we take the standard deviation as the estimated systematic uncertainty on ΔIndex.
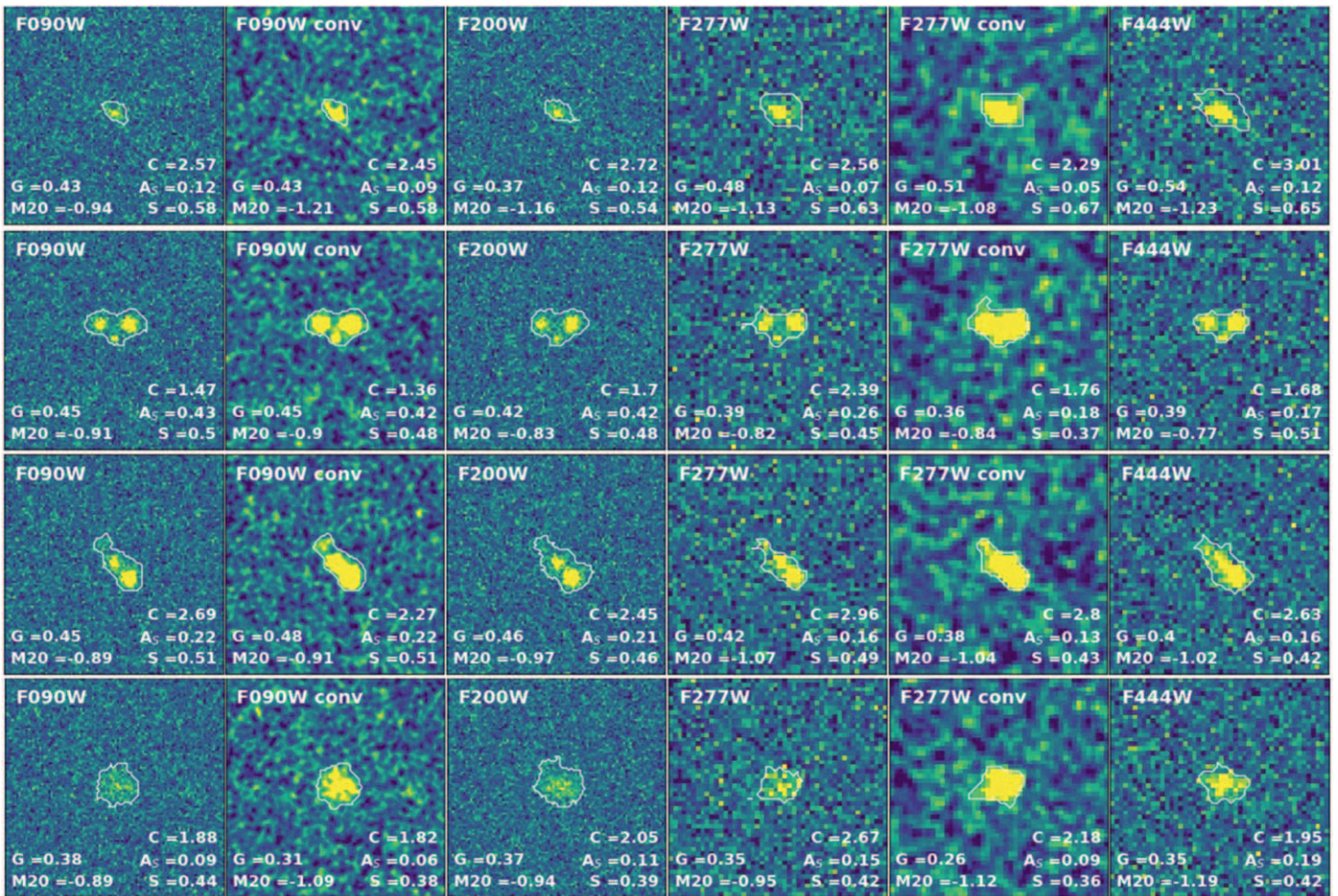
Figure 3. Examples of the simulations carried out to estimate the systematic errors arising from the effects of sampling and correlated noise. A wide range of brightnesses and configurations were considered (see text), beyond those shown here. The stamps are 2″ on a side. Images labeled "F090W conv" and "F277W conv" have been degraded to the resolution of the F200W and F444W band images, respectively.

We summarize in Table 1 the uncertainties on all the parameters for three different values of the object's total magnitude. We find that, as expected, systematic uncertainties increase with total magnitude on average, except smoothness, which remains constant.

Consistent with the previous findings of Lotz et al. (2004) for HST, we find that the indices are systematically affected by the S/N of the images. In our simulations, we find that Gini increases with the average S/N per pixel estimated inside the segmentation maps of the galaxies. In contrast, M_{20}, S, A_S, and C decrease with the S/N. In particular, M_{20}, A_S, and C have a rapid variation below a S/N ~ 2, which makes the derivation of a correction factor rather difficult. Therefore, following Lotz et al. (2004), we do not perform measurements when the average S/N per pixel is < 2. In all cases, the parameters become stable above a S/N per pixel of 8. We thus take the values at higher S/Ns per pixel as our "truth" value and then derive differential corrections (as a function of the average S/N per pixel) that we apply to the observed galaxies in each band. We note that we are interested in trends as a function of wavelength for each galaxy. Therefore we do not need to worry about comparing indices for different galaxies with widely different total S/Ns.

Table 1
1σ Uncertainty on ΔIndex (Index − Index$_{F444W}$) for the Five Morphological Parameters Studied in This Paper, as Estimated from Simulations

Mag$_{AB}$	ΔG	ΔM_{20}	ΔC	ΔA_S	ΔS
26	0.02	0.05	0.2	0.015	0.02
27	0.025	0.06	0.3	0.020	0.02
28	0.03	0.08	0.4	0.030	0.02

4. Results

We now investigate how the morphological parameters described in the previous section change across the six bands of the GLASS-JWST ERS survey (excluding F090W, where galaxies drop out), covering 1–5 μm. At our median redshift of ~ 8.4, this allows us to probe the rest-frame range between Lyα and ~ 5000 Å. For the most distant galaxy at $z \sim 12$, the red filter includes light up to 3800 Å.

Figure 4 summarizes our results (The measurements are listed in Table 2). For each index we include a composite panel. The left part shows how ΔIndex (with respect to F444W) varies as a function of rest-frame wavelength λ_{rf}, while the right part shows the collapsed distribution. In order to summarize the distributions in each band, we consider all the galaxies with reliable measurements (i.e., where the S/N per pixel is above 2), and
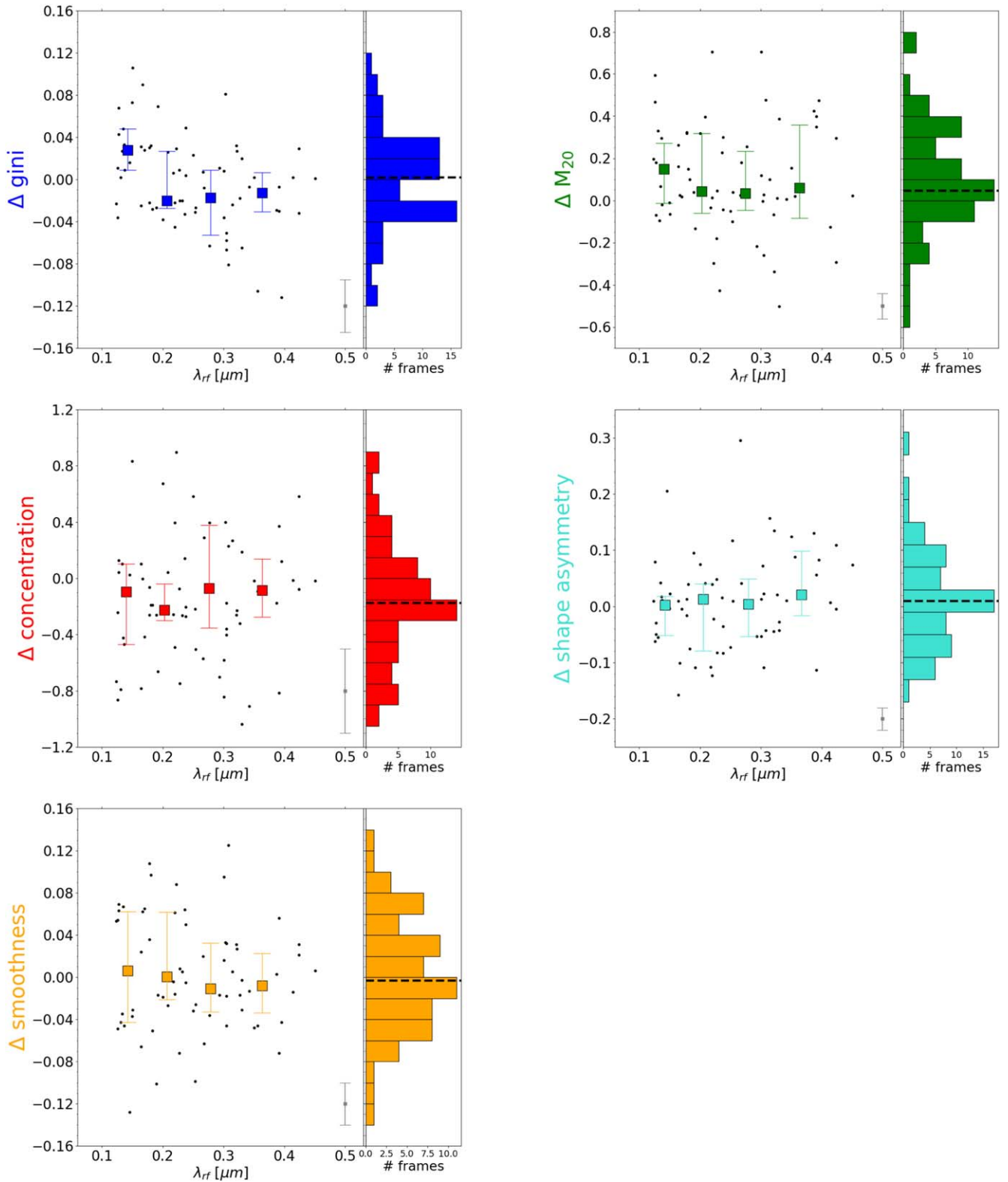
Figure 4. Distribution of ΔIndex (Index − Index$_{F444W}$) for the five morphological parameters presented in the paper as a function of rest-frame wavelength. Each big square in the left plot of each panel represents the median value for the sample, while the error bars represent the first and third interquartiles of the distributions in each bin. The uncertainties on ΔIndex are dominated by the systematic uncertainties summarized in Table 1, which are shown in the bottom right corner of each panel, at the median magnitude of the sample $m_{F444W} \simeq 27$. A histogram of ΔIndex is shown in the right plot of each panel, with the median value as a dashed black line.

compute both the median value of ΔIndex in four equally populated bins of λ_{rf}, and then the first and the third interquartiles of its distribution. These quantities are drawn, respectively, with big colored squares and corresponding vertical error bars.

It is clear that, within our uncertainties and scatter, the morphological indices do not vary dramatically as a function of wavelength across the entire dynamic range probed by our observations. The median ΔIndex is indeed in all cases

Table 2
Table with the Morphological Parameters Estimated for Our Sample

ID	z_{phot}	F115W						F150W						F200W					
		SNpix	gini	M_{20}	C	A_S	S	SNpix	gini	M_{20}	C	A_S	S	SNpix	gini	M_{20}	C	A_S	S
1	10.74	−9.0	−9.0	−9.0	−9.0	−9.0	−9.0	2.8	0.583	−1.582	2.378	0.003	0.107	3.6	0.543	−1.743	1.923	0.047	0.109
2	12.3	−9.0	−9.0	−9.0	−9.0	−9.0	−9.0	−9.0	−9.0	−9.0	−9.0	−9.0	−9.0	3.7	0.605	−1.481	3.569	0.052	0.063
3	11.1478	−9.0	−9.0	−9.0	−9.0	−9.0	−9.0	2.9	0.496	−1.237	2.081	0.097	0.108	3.1	0.494	−1.171	2.032	0.098	0.079
4	10.0814	−9.0	−9.0	−9.0	−9.0	−9.0	−9.0	3.2	0.489	−0.815	1.717	0.156	0.151	3.8	0.473	−0.734	1.95	0.153	0.182
5	9.4055	−9.0	−9.0	−9.0	−9.0	−9.0	−9.0	−9.0	−9.0	−9.0	−9.0	−9.0	−9.0	2.7	0.497	−1.001	1.725	−0.046	0.148
6	9.9013	−9.0	−9.0	−9.0	−9.0	−9.0	−9.0	1.5	−9.0	−9.0	−9.0	−9.0	−9.0	2.6	0.465	−0.915	1.299	0.091	0.089
1470	7.6	1.8	−9.0	−9.0	−9.0	−9.0	−9.0	−9.0	−9.0	−9.0	−9.0	−9.0	−9.0	3.5	0.46	−1.252	1.027	0.653	0.2
2236	8.0	2.7	0.54	−1.638	2.151	0.052	0.065	2.9	0.587	−1.543	2.022	−0.02	0.058	2.4	0.526	−1.867	2.923	0.059	0.084
2574	7.4	2.9	−9.0	−9.0	1.886	−9.0	−9.0	3.1	0.501	−1.36	2.096	0.102	0.106	2.9	0.527	−1.722	2.086	0.053	0.065
2911*	6.9	2.9	0.562	−0.961	1.18	0.29	0.182	3.4	0.519	−1.058	0.894	0.181	0.209	3.7	0.516	−1.197	0.935	0.202	0.211
3120	7.4	3.9	0.462	−0.796	1.567	0.135	−0.009	4.5	0.459	−0.767	1.599	0.102	0.145	4.1	0.478	−0.791	1.461	0.034	0.088
4542	9.0	1.7	−9.0	−9.0	−9.0	−9.0	−9.0	2.5	0.603	−1.723	2.73	0.056	0.07	3.6	0.491	−1.393	2.572	0.134	0.088
4863	8.1	3.0	0.495	−1.182	2.167	0.112	0.054	2.5	0.563	−1.486	2.513	0.018	0.037	3.9	0.486	−1.635	2.805	0.052	0.088
5001	8.1	−9.0	−9.0	−9.0	−9.0	−9.0	−9.0	−9.0	−9.0	−9.0	−9.0	−9.0	−9.0	−9.0	−9.0	−9.0	−9.0	−9.0	−9.0
1708	7.8	3.3	0.517	−1.138	1.95	−0.004	0.09	−9.0	−9.0	−9.0	−9.0	−9.0	−9.0	3.3	0.524	−1.647	2.667	0.099	0.061
4397	8.1	2.3	0.542	−1.072	1.531	0.105	0.15	−9.0	−9.0	−9.0	−9.0	−9.0	−9.0	2.9	0.508	−0.962	1.904	0.065	0.156
6116	8.2	−9.0	−9.0	−9.0	−9.0	−9.0	−9.0	−9.0	−9.0	−9.0	−9.0	−9.0	−9.0	−9.0	−9.0	−9.0	−9.0	−9.0	−9.0
6263	8.2	−9.0	−9.0	−9.0	−9.0	−9.0	−9.0	−9.0	−9.0	−9.0	−9.0	−9.0	−9.0	2.5	0.529	−1.321	2.173	0.027	0.075

ID	z_{phot}	F277W						F356W						F444W					
		SNpix	gini	M_{20}	C	A_S	S	SNpix	gini	M_{20}	C	A_S	S	SNpix	gini	M_{20}	C	A_S	S
1	10.74	6.2	0.482	−1.534	2.48	0.068	0.108	4.6	0.596	−1.764	2.736	0.124	0.077	6.2	0.515	−1.761	2.338	0.052	0.044
2	12.3	6.0	0.525	−1.019	2.094	0.07	0.068	5.6	0.491	−1.237	2.339	0.07	0.032	6.0	0.499	−1.416	2.051	0.029	0.095
3	11.1478	5.6	0.499	−1.387	2.067	0.006	0.064	4.6	0.529	−1.652	2.112	0.035	0.038	4.8	0.519	−1.434	2.814	0.089	0.056
4	10.0814	4.4	0.464	−0.933	2.726	0.041	0.053	3.2	0.473	−0.951	1.88	0.07	0.115	3.9	0.441	−0.883	2.142	0.114	0.085
5	9.4055	6.1	0.435	−0.844	1.818	0.358	0.186	5.9	0.422	−0.861	1.481	0.073	0.152	6.0	0.429	−0.868	2.39	0.063	0.166
6	9.9013	4.1	0.466	−0.976	0.986	0.174	0.115	4.3	0.475	−1.004	1.167	0.187	0.123	5.0	0.493	−1.015	1.49	0.166	0.14
1470	7.6	4.2	0.507	−1.165	1.06	0.477	0.222	4.9	0.482	−0.954	1.276	0.349	0.181	5.2	0.48	−0.827	1.29	0.342	0.195
2236	8.0	4.6	0.416	−1.091	2.252	0.038	0.121	5.2	0.385	−1.094	2.144	0.164	0.047	4.7	0.498	−1.568	2.025	0.081	0.004
2574	7.4	4.4	0.458	−1.292	1.318	0.046	0.04	4.5	0.491	−1.383	2.938	0.198	0.102	4.9	0.523	−1.679	2.356	0.089	0.07
2911*	6.9	5.5	0.549	−0.943	1.136	0.209	0.262	7.3	0.547	−1.074	1.136	0.16	0.316	6.7	0.547	−1.097	1.154	0.085	0.31
3120	7.4	7.1	0.449	−1.593	1.85	0.09	0.034	8.0	0.459	−1.384	1.587	0.113	0.058	7.9	0.429	−1.091	1.663	0.118	0.037
4542	9.0	4.7	0.466	−1.456	2.291	0.058	0.071	4.3	0.423	−1.693	1.806	0.148	0.061	4.1	0.529	−1.712	1.897	0.059	0.108
4863	8.1	4.4	0.48	−0.808	2.009	0.066	0.058	4.6	0.501	−1.297	1.594	0.061	0.031	4.9	0.531	−1.648	2.41	0.175	0.103
5001	8.1	4.2	0.405	−1.17	1.384	0.082	0.08	4.0	0.456	−0.799	2.112	0.137	0.155	4.1	0.463	−1.198	1.743	0.081	0.099
1708	7.8	4.6	0.491	−1.368	3.008	0.208	0.138	−9.0	−9.0	−9.0	−9.0	−9.0	−9.0	7.3	0.515	−1.468	2.74	0.052	0.133
4397	8.1	4.8	0.464	−1.927	2.217	0.049	0.128	−9.0	−9.0	−9.0	−9.0	−9.0	−9.0	5.1	0.531	−1.667	2.394	0.026	0.096
6116	8.2	4.2	0.478	−0.716	1.454	0.073	0.125	5.3	0.442	−0.997	1.86	0.189	0.033	6.7	0.471	−1.421	2.035	0.059	0.03
6263	8.2	4.5	0.486	−1.168	1.589	0.082	0.095	−9.0	−9.0	−9.0	−9.0	−9.0	−9.0	5.3	0.523	−1.286	2.432	0.135	0.079

Note. * = This measurement actually refers to the two interacting galaxies ID 2911 and 2936 in the catalog of Leethochawalit et al. (2022).

consistent with zero within its 1σ uncertainty. However, in order to quantify the potential significance of any observed trends, we need to carry out a regression analysis, accounting for the uncertainties, estimated as in Section 3.

Overall, we do not find significant variations of ΔIndex as a function of wavelength, indicating that the properties of our galaxies across all the bands from far-UV to optical rest frame do not change significantly. We also note that the distribution of ΔIndex is approximately Gaussian around the median values for all the parameters, and their FWHM are consistent with the level of uncertainty estimated from the simulations for each ΔIndex.

It is also worth looking at the trends within individual galaxies, to identify systems where the indices depend more strongly on wavelength, even though we expect that such trends would be more noisy compared to the previous average analysis. For this purpose, we consider for each galaxy the slope of ΔIndex versus $\lambda_{\rm rest-frame}$ with the available bands, and the median ΔIndex. We find that the slope is not significantly different from 0 on average, and the median varies by less than the systematic uncertainty. There are however a few exceptions where a significant dependency on wavelength is found. Galaxy ID 2911, an interacting system, has a higher smoothness and lower shape asymmetry at longer wavelengths, while galaxy ID 2236 has the opposite trend for the smoothness and shape asymmetry, and also a $>3\sigma$ significant morphological diversity as a function of λ of Gini and M_{20}. Finally, the scatter of ΔIndex in individual galaxies is in general comparable to its uncertainty, and we do not see correlations among the parameters in the same galaxy.

Furthermore, we also do not find in general a significant shift in the galaxy centroid between F444W and the bluest band available. However, we obtain small shifts (between 400 and 800 pc) for $\sim$15% of the sample, which might be due in part to clumps having a different spectral energy distribution, as for galaxy ID 4397.

Overall, we conclude that the variations of all the indices from far-UV to optical rest frame are certainly not dramatic, as we might have expected if the UV light corresponds to a small star-forming region within a much larger galaxy as traced by older or dust-obscured stars.

Finally, we analyse more in detail the effect of PSF smoothing. Deriving morphological parameters from images PSF-matched to the F444W band does not introduce significant differences for most of the indices. The exceptions are Gini and concentration, for which we find that, while there is still no correlation with $\lambda_{\rm rest}$ in Figure 4, ΔIndex is systematically lower by $\sim$0.04 and $\sim$0.4, respectively, if they are measured on the smoothed images. The effect is also seen in our simulations.

5. Discussion and Comparison with Previous Work

5.1. Morphology as a Function of Wavelength

We have shown in the previous section that at $z > 7$ the morphological indices do not vary significantly between the UV and optical. This behavior is different from that reported by previous studies at $z \sim 3$–4 and a far cry from the most extreme examples at lower redshift.

At $z \sim 3$–4, Conselice et al. (2008) and Wuyts et al. (2012) find that typical star-forming galaxies in the optical rest frame have on average slightly smaller M_{20}, and a higher concentration and Gini coefficients than in the UV by $\sim$0.3, 0.1, and 0.3,

respectively, i.e., 1–3 times larger differences than our systematic uncertainties. This means that if similar variations are present at $z > 7$, we would have been able to detect them. These trends at $z \sim 3$–4 are explained as evidence for disk assembly through the inward migration of clumps and gas accretion. However, other similar studies report much milder or no morphological transformations with wavelength at $z \sim 2.5$ (Dickinson 1999; Papovich et al. 2005), which might be due in part to selection effects as their galaxies are bluer, with both UV and optical emission dominated by recent star formation. Similarly, Bond et al. (2011) claim that morphological differences between the rest-frame optical and UV in typical star-forming galaxies at $1.4 < z < 3$ are small, which are likely due to uniform dust distributions. As we discuss below, we believe that a version of these arguments—exacerbated by the extreme conditions at $z > 7$—is a possible explanation for our results.

In contrast, in the most extreme examples at low to intermediate redshifts ($z \lesssim 1$), larger differences with wavelength arise from inhomogeneity in the distribution of recent star formation (Elmegreen et al. 2009; Rawat et al. 2009), which typically occurs inside a disk with a larger scale length, and with the possible contribution from bright, off-centered clumps, or from patchy dust obscuration.

We now describe multiple factors that we believe contribute to the absence of a strong wavelength dependency of the morphology.

First, galaxies at $z = 7$–12 have had very little time to form stars, since the universe is only 400–800 Myr old at this point. Therefore, by necessity there cannot be much spectral difference between the oldest stars and the ones that dominate the UV emission. Color trends are compressed by the timescale of the universe.

Second, the galaxies in our sample are vigorously star forming and are not heavily dust obscured, owing to a combination of young ages and the Lyman-break selection technique (Jaacks et al. 2018). Therefore, they did not have the time to build a substantial population of old stars, nor had the dust to hide a large fraction of young stars.

Third, in the Lyman-break galaxies at these redshifts, star formation seems to be a global phenomenon, encompassing the majority of the galaxy, and not confined to a disk-like structure, or in isolated star-forming regions, like in the local universe.

Fourth, if the star formation rate is smoothly rising as suggested by a number of authors (Finlator et al. 2011), most of the stars have recently formed, further reducing the time span available to give rise to morphological differences. For example, Finlator et al. (2011) predict that for this kind of star formation history, optically and UV-selected samples should be coincident, which would be consistent with the observed morphologically uniformity.

In conclusion, our results are qualitatively consistent with a scenario where Lyman-break galaxies at $z > 7$ are growing via galaxy-scale star formation. Detailed analyses of larger samples and multiwavelength follow-up (especially with the Atacama Large Millimeter/submillimeter Array (ALMA) and with spectroscopy) are needed to reach a quantitative understanding of the relative contribution of these factors. This is left for future work.

Our results are consistent with those presented by Yang et al. (2022b) in a companion paper (paper V in this series). They carry out detailed surface photometry of the sample presented

here, and they do not find any major variation in the size–luminosity relation as a function of wavelength. This is at odds with the expectations of larger UV sizes coming from predictions of inside-out disk assembly models at high-redshift (Dutton et al. 2011). In turn, this suggests that the physical effects responsible for our patterns cannot be reconducted to the typical bulge—disk dichotomy emerging at lower redshift.

A major caveat of our work, of course, is selection effects. In this first exploratory look, we have selected galaxies primarily following the Lyman-break technique. In some sense we have selected "normal" and common star-forming galaxies. This selection is heavily biased against dust-enshrouded or quiescent galaxies. We do not know yet whether they exist at these redshifts. If they do, they will clearly not display the same amount of morphological regularity across the wavelengths that we see in our sample. Observations at even longer wavelengths, such as those with ALMA (Inami et al. 2022), will provide invaluable insights. Similarly, samples that are selected via emission lines, as opposed to the continuum, may reveal more morphological differences. JWST observations of samples selected in complementary ways may alter this first impression of morphological uniformity.

A second caveat is that these are just the first deep NIRCAM images, consisting of approximately 6 hr of exposure at F444W and less than 2 hr at F356W (Treu et al. 2022). Already the NIRSPEC parallels of GLASS-JWST will be deeper and it is not difficult to imagine integrating ten times as long in a deep field, once the instrument artifacts are properly understood (Merlin et al. 2022). Deeper images may reveal more morphological differences at lower surface brightnesses.

A third caveat is that these galaxies are extremely compact, with radii of just a few 100 pc (Paper V). They did not have to be so compact in the optical, but since they are, there could be smaller-scale morphological differences that are below even JWST's resolution. Highly magnified sources will be valuable to overcome this limitation.

5.2. Visual Morphology and Merger Identification

Consistent with the uniformity of morphological indices as a function of wavelength, we also do not observe a dramatic change of the visual morphology of the galaxies in our sample (Figures 1 and 2).

However, we notice that there is a diversity of shapes across the sample. Some of them are more compact, some of them are more elongated, and some of them have nearby companions, suggesting interactions or the accretion of clumps. We leave a detailed exploration of the distribution of visual morphology to future work, when larger samples will be available at the end of the GLASS-JWST campaign. For the time being, we only comment on a few remarkable objects.

Four of our 19 galaxies are consistent with being interacting systems ($21\% \pm 10\%$; IDs 6, 1470, 2911, and 2936). The first galaxy likely has a close and faint companion lying within its segmentation map. In the other two cases, the interactions are outside of the segmentation maps, thus we can actually check the photometric redshift of the companions. We also center the cutouts in the asymmetry center of the interacting systems in these cases. For galaxy ID 1470, we notice three closely separated objects with a relative distance of less than $1''.0$ The two galaxies on the left have photometric redshifts of 7.6 and 6.9, consistent within their uncertainties, while the object on the right is likely an interloper with a $z_{\mathrm{phot}} = 0.55$. ID 2911 is a

bright, interacting system with a (photometric) redshift $\simeq 7$. We note that the fraction of the interacting systems in our sample is similar to that of merging pairs identified by Conselice & Arnold (2009) among i-band dropouts at $z \sim 6$ in the Hubble Ultra Deep Field.

One galaxy (ID 4397) has a clumpy structure clearly visible in all the available bands, from F115W to F444W.

The remaining galaxies of our sample appear instead isolated. In those few cases where a companion system is observed in the same cutout, we find that they are likely low-redshift interlopers.

Statistical comparison with previous work at lower redshift requires a detailed assessment of incompleteness. It would be premature to carry out such a study given our sample size. We leave this effort for future work, after the completion of the survey.

6. Conclusions

JWST has given us new eyes to study the universe at $z > 7$. For the first time, we have access to images of sufficient depth and resolution to characterize the morphology of galaxies deep into the reionization era, when galaxies were just 400–800 Myr old. In this letter, we have exploited NIRCAM data taken as part of the GLASS-JWST program to take a first look. The main results are as follows:

1. The morphologies of Lyman-break galaxies do not change significantly with wavelength, going from rest-frame optical to rest-frame UV.
2. Four out of 19 galaxies in our sample present clear signs of interaction or accretion.

We suggest a possible scenario that could at least qualitatively explain the observations. These galaxies are undergoing rapid, galaxy-scale star formation. The timescales are extremely compressed given the young age of the universe and the likely rising star formation rate (Finlator et al. 2011), leaving little time for the emergence of older stellar populations. Their compact sizes mean that crossing times are short (1–10 Myr for speeds of order 10–100 km s^{-1}) compared to the spread in age of stellar populations that would be required to see a major difference, and therefore they are likely well mixed. Dust extinction is not sufficient in quantity or patchiness to induce detectable differences. The clear detection of interacting systems is consistent with merging also contributing to the growth of these galaxies.

We conclude by listing some caveats that should be kept in mind and which prevent us from drawing more quantitative conclusions at this time. First, our sample is small, and with a very clear selection function. Studies of galaxies selected at different wavelengths or through emission lines may reveal more morphological diversity as a function of wavelength. Second, the GLASS-JWST images are relatively deep but by no means the deepest that one can obtain with JWST. Already our second set of images will be significantly deeper. It is possible that deeper imaging may reveal lower surface brightness features that have escaped our detection. Third, these galaxies are compact, as shown in companion Paper V, a few resolution elements across even with JWST. They did not have to be so compact in the optical rest frame—and this is an important result—but we cannot rule out more morphological diversity at even higher resolution. Studies of highly magnified galaxies will be very helpful in this respect.

We plan to address some of the limitations identified here and carry out a detailed comparison with lower redshift work based on HST and JWST in the near future, after the completion of the GLASS-JWST observations.

ORCID iDs

T. Treu ⓘ https://orcid.org/0000-0002-8460-0390
A. Calabrò ⓘ https://orcid.org/0000-0003-2536-1614
M. Castellano ⓘ https://orcid.org/0000-0001-9875-8263
N. Leethochawalit ⓘ https://orcid.org/0000-0003-4570-3159
E. Merlin ⓘ https://orcid.org/0000-0001-6870-8900
A. Fontana ⓘ https://orcid.org/0000-0003-3820-2823
L. Yang ⓘ https://orcid.org/0000-0002-8434-880X
T. Morishita ⓘ https://orcid.org/0000-0002-8512-1404
M. Trenti ⓘ https://orcid.org/0000-0001-9391-305X
A. Dressler ⓘ https://orcid.org/0000-0002-6317-0037
C. Mason ⓘ https://orcid.org/0000-0002-3407-1785
D. Paris ⓘ https://orcid.org/0000-0002-7409-8114
L. Pentericci ⓘ https://orcid.org/0000-0001-8940-6768
G. Roberts-Borsani ⓘ https://orcid.org/0000-0002-4140-1367
B. Vulcani ⓘ https://orcid.org/0000-0003-0980-1499
K. Boyett ⓘ https://orcid.org/0000-0003-4109-304X
M. Bradac ⓘ https://orcid.org/0000-0001-5984-0395
K. Glazebrook ⓘ https://orcid.org/0000-0002-3254-9044
T. Jones ⓘ https://orcid.org/0000-0001-5860-3419
D. Marchesini ⓘ https://orcid.org/0000-0001-9002-3502
S. Mascia ⓘ https://orcid.org/0000-0002-9572-7813
T. Nanayakkara ⓘ https://orcid.org/0000-0003-2804-0648
P. Santini ⓘ https://orcid.org/0000-0002-9334-8705
V. Strait ⓘ https://orcid.org/0000-0002-6338-7295
E. Vanzella ⓘ https://orcid.org/0000-0002-5057-135X
X. Wang ⓘ https://orcid.org/0000-0002-9373-3865

References

Abraham, R. G., Tanvir, N. R., Santiago, B. X., et al. 1996, MNRAS, 279, L47
Abraham, R. G., van den Bergh, S., & Nair, P. 2003, ApJ, 588, 218
Bond, N. A., Gawiser, E., & Koekemoer, A. M. 2011, ApJ, 729, 48
Bowler, R. A. A., Dunlop, J. S., McLure, R. J., & McLeod, D. J. 2017, MNRAS, 466, 3612
Castellano, M., Fontana, A., Treu, T., et al. 2022, ApJL, in press (arXiv:2207.09436)
Conselice, C. J. 2014, ARA&A, 52, 291
Conselice, C. J., & Arnold, J. 2009, MNRAS, 397, 208
Conselice, C. J., Bershady, M. A., Dickinson, M., & Papovich, C. 2003, AJ, 126, 1183
Conselice, C. J., Rajgor, S., & Myers, R. 2008, MNRAS, 386, 909
Dickinson, M. 1999, in AIP Conf. Ser. 470, After the Dark Ages: When Galaxies were Young (the Universe at $2 < Z < 5$), ed. S. Holt & E. Smith (Melville, NY: AIP), 122
Doyon, R., Hutchings, J. B., Beaulieu, M., et al. 2012, Proc. SPIE, 8442, 84422R
Dutton, A. A., van den Bosch, F. C., Faber, S. M., et al. 2011, MNRAS, 410, 1660
Elmegreen, B. G., Elmegreen, D. M., Fernandez, M. X., & Lemonias, J. J. 2009, ApJ, 692, 12
Finlator, K., Oppenheimer, B. D., & Davé, R. 2011, MNRAS, 410, 1703
Grazian, A., Castellano, M., Fontana, A., et al. 2012, A&A, 547, A51
Hubble, E. P. 1926, ApJ, 64, 321
Huertas-Company, M., Bernardi, M., Pérez-González, P. G., et al. 2016, MNRAS, 462, 4495
Inami, H., Algera, H., Schouws, S., et al. 2022, MNRAS, 515, 3126
Jaacks, J., Finkelstein, S. L., & Bromm, V. 2018, MNRAS, 475, 3883
Jacobs, C., Glazebrook, K., Calabrò, A., et al. 2022, arXiv:2208.06516
Kuchinski, L. E., Madore, B. F., Freedman, W. L., & Trewhella, M. 2001, AJ, 122, 729
Law, D. R., Steidel, C. C., Shapley, A. E., et al. 2012, ApJ, 745, 85
Lee, B., Giavalisco, M., Williams, C. C., et al. 2013, ApJ, 774, 47
Leethochawalit, N., Trenti, M., Santini, P., et al. 2022, ApJL, in press (arXiv:2207.11135)
Lotz, J. M., Primack, J., & Madau, P. 2004, AJ, 128, 163
Merlin, E., Bonchi, A., Paris, D., et al. 2022, ApJL, in press (arXiv:2207.11701)
Morishita, T., Ichikawa, T., & Kajisawa, M. 2014, ApJ, 785, 18
Oesch, P. A., Bouwens, R. J., Carollo, C. M., et al. 2010, ApJL, 709, L21
Papovich, C., Dickinson, M., Giavalisco, M., Conselice, C. J., & Ferguson, H. C. 2005, ApJ, 631, 101
Pawlik, M. M., Wild, V., Walcher, C. J., et al. 2016, MNRAS, 456, 3032
Rawat, A., Wadadekar, Y., & De Mello, D. 2009, ApJ, 695, 1315
Ribeiro, B., Le Fèvre, O., Tasca, L. A. M., et al. 2016, A&A, 593, A22
Rieke, M. J., Kelly, D., & Horner, S. 2005, Proc. SPIE, 5904, 1
Roberts-Borsani, G., Morishita, T., Treu, T., et al. 2022, ApJL, in press (arXiv:2207.11387)
Shibuya, T., Ouchi, M., & Harikane, Y. 2015, ApJS, 219, 15
Treu, T., Roberts-Borsani, G., Bradac, M., et al. 2022, ApJ, 935, 110
van der Wel, A., Franx, M., van Dokkum, P. G., et al. 2014, ApJ, 788, 28
Whitney, A., Ferreira, L., Conselice, C. J., & Duncan, K. 2021, ApJ, 919, 139
Wuyts, S., Förster Schreiber, N. M., Genzel, R., et al. 2012, ApJ, 753, 114
Yang, L., Leethochawalit, N., Treu, T., et al. 2022a, MNRAS, 514, 1148
Yang, L., Morishita, T., Leethochawalit, N., et al. 2022b, ApJL, in press (arXiv:2207.13101)